

# Automated correction of fast motion artifacts for two-photon imaging of awake animals

David S. Greenberg\*, Jason N.D. Kerr\*

Network Imaging Group, Max Planck Institute for Biological Cybernetics, Spemannstraße 41, 72076 Tübingen, Germany

## ARTICLE INFO

### Article history:

Received 17 April 2008

Received in revised form 11 August 2008

Accepted 12 August 2008

### Keywords:

Motion correction  
Two-photon imaging  
Awake optical recording  
Brain motion  
Action potential  
Image registration  
Raster scan  
Head-fixed

## ABSTRACT

Two-photon imaging of bulk-loaded calcium dyes can record action potentials (APs) simultaneously from dozens of spatially resolved neurons *in vivo*. Extending this technique to awake animals, however, has remained technically challenging due to artifacts caused by brain motion. Since in two-photon excitation microscopes image pixels are captured sequentially by scanning a focused pulsed laser across small areas of interest within the brain, fast displacements of the imaged area can distort the image nonuniformly. If left uncorrected, brain motion in awake animals will cause artifactual fluorescence changes, masking the small functional fluorescence increases associated with AP discharge. We therefore present a procedure for detection and correction of both fast and slow displacements in two-photon imaging of awake animals. Our algorithm, based on the Lucas–Kanade framework, operates directly on the motion-distorted imaging data, requiring neither external signals such as heartbeat nor a distortion-free template image. Motion correction accuracy was tested *in silico* over a wide range of simplified and realistic displacement trajectories and for multiple levels of fluorescence noise. Accuracy was confirmed *in vivo* by comparing solutions obtained from red and green fluorophores imaged simultaneously. Finally, the accuracy of AP detection from motion-displaced bulk-loaded calcium imaging is evaluated with and without motion correction, and we conclude that accurate motion correction as achieved by this procedure is both necessary and sufficient for single AP detection in awake animals.

© 2008 Elsevier B.V. All rights reserved.

## 1. Introduction

Two-photon imaging (Denk et al., 1990) has proven uniquely effective in monitoring neuronal activity *in vivo* (for a recent review see Kerr and Denk, 2008). More recently, laser scan excitation of bulk-loaded calcium indicators (Stosiek et al., 2003) has allowed action potential (AP) detection in dozens of neurons simultaneously, hundreds of micrometers below the brain surface (Kerr et al., 2005, 2007; Sato et al., 2007). APs cause a calcium influx through voltage-gated ion channels, resulting in fluorescence increases across neuronal cell bodies that can be transformed back into APs algorithmically, with single-AP resolution and a low error rate (Greenberg et al., 2008). Because the resulting AP evoked calcium transients are relatively small, movement of the brain during data collection must be kept to a minimum. This requirement has restricted neuronal imaging mainly to the anesthetized animal, and imaging in awake head-fixed animals poses a new set of motion artifact based problems that need to be overcome. Correct-

ing motion-associated artifacts is greatly complicated by the fact that two-photon imaging does not acquire the pixel fluorescence values composing an image simultaneously, but rather sequentially as the beam focus is moved in a scan pattern across the imaging plane. Since pixels are separated in both space and time, fast brain displacements arising from movement of the animal will affect separate parts of one imaging frame differently, producing motion artifacts that cannot be corrected by moving, stretching, or rotating entire imaging frames.

We present here a technique for automated detection and correction of both fast and slow displacements in two-photon imaging of neuronal population activity in awake head-fixed rats. Our method is based on the Lucas–Kanade image registration algorithm (Lucas and Kanade, 1981, for a review see Baker and Matthews, 2004) and estimates complex displacement trajectories occurring within individual image frames by gradient descent. The procedure operates “blind,” relying only on sequences of imaging frames without measurement of the animal’s movements, heartbeat, respiration, or muscular tension, and does not require collection of an undistorted reference frame for use as a template. We describe several optimizations to maximize speed and accuracy and investigate computational costs theoretically and empirically. A procedure is derived for assigning true pixel positions applicable even when

\* Corresponding authors.

E-mail addresses: [david@tuebingen.mpg.de](mailto:david@tuebingen.mpg.de) (D.S. Greenberg), [jason@tuebingen.mpg.de](mailto:jason@tuebingen.mpg.de) (J.N.D. Kerr).

every frame is heavily motion-distorted, allowing us to determine true distances in microns between image features even when these distances are altered in all individual frames. We test the limits of the technique with respect to displacement type, displacement amplitude, and noise levels using *in silico* simulations and *in vivo* experimental controls, describe ongoing brain motion in awake animals, and conclude that correcting the displacements occurring in awake head-fixed rats with sub-pixel and sub-micron resolution is well within the capabilities of the method. Finally, the effects of corrected and uncorrected displacement on the optical detection of action potential (AP) activity in individual neurons using fluorescence signals from bulk-loaded calcium indicator are examined. We show that action potential related transients can be completely obscured by brain motion, but that motion correction successfully recovers these transients, thereby allowing accurate detection of single APs.

## 2. Materials and methods

### 2.1. Raw data

All the data from awake animals used to test the performance of this algorithm were from a previously published study (Greenberg et al., 2008). In addition, both cell-attached and whole-cell electrical recordings were performed as previously described (Kerr et al., 2005). Unless otherwise noted, imaging consisted of  $64 \times 128$  pixel frames collected over 96 ms each.

### 2.2. *In silico* displacement correction tests

Displacement angle was varied in  $45^\circ$  increments. 80 random and uniformly distributed values for phase and latency were used to determine convergence probability and estimation error for sinusoids and impulses, respectively. Each data point from *in silico* tests for correction of motion trajectories detected *in vivo* consisted of motion trajectories from 500 randomly selected imaging frames. Motion correction used  $n = 32$  linear segments per trajectory unless otherwise noted. Thus for  $64 \times 128$  imaging frames collected over 96 ms each, each linear segment was 3 ms in duration, while error was minimized over all pixels.

### 2.3. Image processing and interpolation

All images were Gaussian-filtered prior to displacement estimation, with a standard deviation of 0.65 pixels in the  $x$  and  $y$  directions, in order to reduce noise in fluorescence measurements. Images are displayed unfiltered. Sampling an image or a time-displacement function at a precise location in an image was defined as the bilinear interpolation between the values of the image or displacement function at the four pixels surrounding that location (see Appendix A). Correlation between two images was defined as the standard scalar-valued Pearson correlation coefficient taken over all image pixels.

### 2.4. Full-frame translation estimations

To estimate optimal translations between an image  $I$  and a template  $T$  as candidates for initial displacement estimates, we first padded  $I$  and  $T$  with zeros along the  $x$  and  $y$  directions, such that their widths became  $\text{width}(I) + \text{width}(T) - 1$  and their heights became  $\text{height}(I) + \text{height}(T) - 1$ . Next, we smoothed  $I$  with 1.5 pixel Gaussian filters in the  $x$  and  $y$  direction. We then rotated  $I$  by  $180^\circ$  to form a new image  $I'$ . Finally we took the 2D fast Fourier transforms  $F(I')$  and  $F(T)$ , and set  $W = \text{Re}\{F^{-1}(F(I') \cdot F(T))\}$ , where  $\text{Re}\{\dots\}$  denotes

real part and  $\text{conj}(\dots)$  denotes complex conjugate. The (integer) coordinates of the maximum of  $W$  give the full frame translation to be used as a candidate for  $p^0$ .

### 2.5. Calculation of fluorescence kinetics for motion-corrected data

In motion-corrected data, a single pixel of a given region of interest (ROI) might not be sampled in all frames, since displacement may cause gaps to appear in individual images and may also cause pixels to be present in some frames and outside the field of view in others. A simple average over all ROI pixels sampled in each frame is not appropriate, since it would show fluorescence changes in the absence of functional fluorescence changes depending on whether the brighter or darker pixels are present in each frame. Instead, we first calculated for each pixel  $i$  in the ROI the mean fluorescence  $F_{\text{ROI}}(i)$  of that pixel over all frames in which it is present. Next, denoting the set of ROI pixels by  $S$  and the set of pixels present in frame  $j$  by  $S_j$ , for each frame  $j$  we calculated the normalization factor  $N(j) = \left( (1/|S_j|) \sum_{i \in S_j} F_{\text{ROI}}(i) \right) / \left( (1/|S|) \sum_{i \in S} F_{\text{ROI}}(i) \right)$ , where  $| \cdot |$  denotes the number of elements in a set. We then divided the mean fluorescence over all pixels in frame  $j$  by  $N(j)$  to obtain a normalized fluorescence measurement for frame  $j$ . Further analysis of fluorescence signals for the calculation of baseline and  $\% \Delta F/F_0$  and detection of APs then proceeded as described in previous work (Greenberg et al., 2008).

### 2.6. Software implementation

Software routines for detection and correction of displacement, as well as those used for data analysis were written in Matlab (Mathworks). C subroutines were used for some spike detection operations where speed was essential, but all displacement estimation and motion correction operations were executed in Matlab.

## 3. Results

### 3.1. Raster scanning

A two-photon microscope produces a sequence of image frames by passing a focus of laser excitation repeatedly over a rectangular or square region of fluorescently labeled tissue and collecting the resulting photons via a photon multiplier tube (PMT) (Fig. 1a). In brain tissue bulk-loaded with a calcium sensitive fluorescent indicator, neuronal somata are clearly visible in two-photon images as brighter than the surrounding background (Fig. 1a, bottom left). Optical detection of action potentials relies on observing fluorescence changes in the pixels corresponding to each soma. Ideally, a pixel value of an image  $I$  (Fig. 1a, bottom left) corresponds to the intensity of fluorescence collected as a known point in the imaged brain tissue  $T$  (Fig. 1a, bottom right) is excited by the focus:  $I(x(t), y(t)) = T(x(t), y(t))$  (a list of all variables is given in Table 1). Thus, the pixel value assigned at time  $t$  is determined from the fluorescence collected while exciting the corresponding point in the tissue. To obtain a rectangular image  $w$  pixels wide and  $h$  pixels high, the focus traverses a raster scan pattern (Fig. 1a, top left), moving in a sawtooth pattern in the  $x$  dimension and a step function in  $y$  dimension:

$$x(t) = \left\{ \frac{t}{(\tau/h)} \right\} \cdot w \quad (1)$$

$$y(t) = \left\lfloor \frac{t}{(\tau/h)} \right\rfloor \quad (2)$$

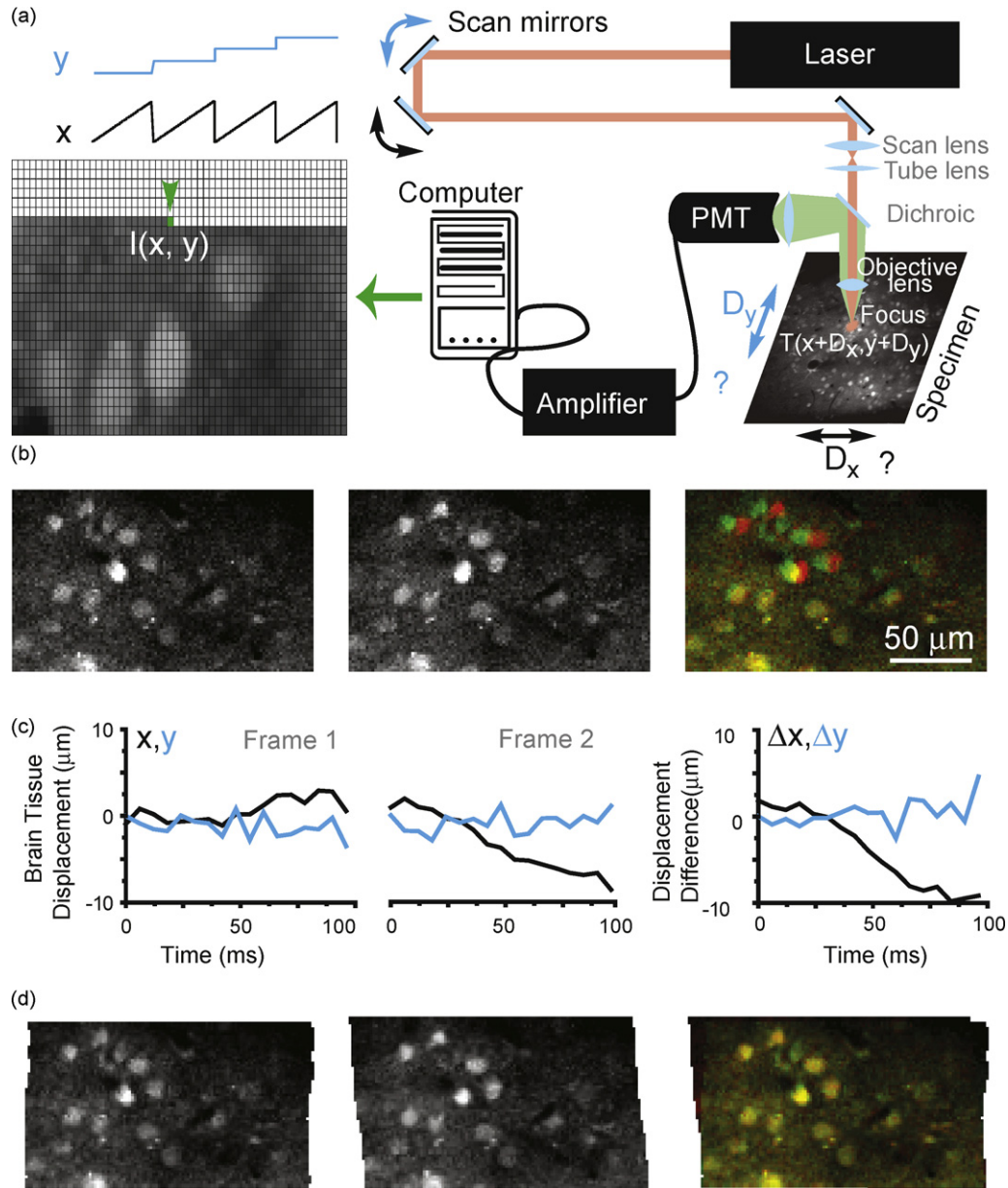


**Fig. 1.** Detection and correction of motion artifacts in raster scanned data. (a) Diagram illustrating raster scan acquisition of functional imaging data. Laser light (red) is deflected from scan mirrors and focused onto a specimen, exciting a fluorophore which then emits light at another wavelength (green). Emitted light is separated with a dichroic filter and measured with a photomultiplier tube. Scan mirrors move continuously to position the excitation focus at the desired location, passing through each point in the desired field of view once per frame. However, additional movement of the imaged tissue can cause incoming fluorescence data to be assigned to the wrong location. (b) Observation of an *in vivo* within-frame motion artifact in L2/3 visual cortex of an awake rat, using two-photon excitation of the calcium indicator OGB1-AM. Two images (left, center) were raster scanned over consecutive 96 ms periods. Overlaying the two consecutive images (right, first image green, second image red) shows they agree for the bottom part of the frame, but not for the top part, indicating that the specimen was displaced relative to the microscope during one or both frames. (c) Displacement of the specimen in the x (black) and y (cyan) directions relative to the desired scan pattern during both 96 ms frames (left, center), estimated by an alignment algorithm (see text). Displacement difference between the two frames (right). (d) Corrected images with fluorescence values assigned to the positions estimated by the alignment algorithm for the two frames shown in (b) (left, center). Overlay of the corrected images, showing good agreement throughout the frame (right).

where  $\lfloor \dots \rfloor$  and  $\{ \dots \}$  denote the integer (rounded down) and fractional parts of a number, while  $\tau = wh \cdot t_{\text{pixel}}$  is the duration in which a single image is obtained. In the following we discretized time with resolution  $t_{\text{pixel}}$ , the duration of a single pixel. The pixels are collected at times  $(0.5 \cdot t_{\text{pixel}}, 1.5 \cdot t_{\text{pixel}}, 2.5 \cdot t_{\text{pixel}}, \dots, \tau - 0.5 \cdot t_{\text{pixel}})$  as the scan is carried out from  $t = 0$  to  $t = \tau$ .

### 3.2. The effect of brain displacement

When the tissue is stationary relative to the microscope the ideal case described above is achieved and a neuron occupies the same

pixels in each frame. In practice, however, this is not always the case. For awake animals, even in images collected in immediate succession (Fig. 1b left and center,  $\tau = 96$  ms, no pause between images) neurons may have different locations (Fig. 1b, right). Note in that in this example, the initial (bottom) portion of the two frames matches while the latter (upper) portion does not, indicating tissue displacement on a shorter timescale than the scan pattern duration  $\tau$ . We must therefore revise our description of the relationship between the image obtained and the true distribution of fluorescence in the imaged tissue:  $I(x(t), y(t)) = T(x(t) + D_x(t), y(t) + D_y(t))$ , where  $D_x, D_y$  are displacement trajectories unknown to the experimenter. The

aim of the present work is to determine the trajectories  $D_x$  and  $D_y$  (Fig. 1c) and use them to assign pixels in the image  $I$  to the correct locations in the brain tissue  $T$  (Fig. 1d, left and center). Successfully inferring the displacement trajectories allows alignment of corrected imaging frames (Fig. 1d, right), determination of which pixels a neuron occupies in each uncorrected frame, and ultimately accurate inference of AP activity from changes in fluorescence in awake animals.

### 3.3. Displacement estimation and correction

We first developed a procedure to estimate  $D_x$ , and  $D_y$  given a displacement-distorted image  $I$  and a displacement-free template image  $T$  (a procedure to generate  $T$  requiring only displacement-distorted images is described later). For the purposes of AP detection,  $I$  will be an image collected from an awake animal with  $\tau \leq 100$  ms, while  $T$  is obtained during subsequent anesthesia. Because  $T$  is not used to determine AP times but only for structural information, it is practical for  $T$  to be captured over a longer duration; therefore more area can be covered with greater spatial resolution and multiple images can be averaged to increase signal-to-noise ratio. Note that we are correcting only lateral brain motion (in the  $x$ - and  $y$ -dimensions), whereas axial motion (along the  $z$ -axis) is not correctable in the same way since neurons vanish upon moving completely out of the focal plane. Fortunately, however, awake animals display much greater lateral than axial brain motion, and only a small fraction of imaging data must be rejected due to movement of the brain along the  $z$ -axis (see, Section 3.7).

Since we cannot observe displacement directly, we instead look for the best match between the template and the motion corrected data. We do this by choosing the trajectories  $D_x$ , and  $D_y$  that minimize the square difference  $E$  between pixel values of the captured image and pixel values of the template at the positions of estimated displacement:

$$E = \sum_t [T(x(t) + D_x(t), y(t) + D_y(t)) - I(x(t), y(t))]^2 \quad (3)$$

where  $t$  ranges over pixel acquisition times. That is, we are searching for the displacement trajectory that gives the best match between the resampled template and the distorted image. The problem of solving for arbitrary displacements ( $D_x(t)$ ,  $D_y(t)$ ) for every pixel is severely underconstrained, since we would then have  $wh$  pixel fluorescence values from our data and  $2wh$  unknown displacement values for which to solve. Instead, we must choose some family of time-displacement functions that is general enough to provide a close match to the true displacements occurring in imaging frames, but is also described by a small number of parameters. In this way we can obtain a good estimate for the displacement trajectory by solving an overconstrained problem for a small number of unknown values. In the following we will consider a vector of parameters  $p$  with the  $i$ th parameter denoted  $p_i$ .

For simplicity, we used a basic “downsampling parameterization” (other possible parameterizations are discussed in Section 4). We took as parameters for  $D$  the  $x$ - and  $y$ -displacements at  $n+1$  time points separated by divisions of  $\tau/n$ :  $t_1=0$ ,  $t_2=\tau/n$ ,  $t_3=2\tau/n$ , ...,  $t_{n+1}=\tau$ , and interpolated  $D$  linearly between these time points. Thus the first  $n+1$  parameters describe  $x$ -displacement and the remaining  $n+1$  describe  $y$ -displacement, so that  $p$  will be a  $2n+2$  dimensional vector. Thus for  $t_i < t < t_{i+1}$  we have:

$$\begin{aligned} D_x(t) &= p_i + (p_{i+1} - p_i)(t - t_i)/(\tau/n), \\ D_y(t) &= p_{i+n+1} + (p_{i+n+2} - p_{i+n+1})(t - t_i)/(\tau/n) \end{aligned} \quad (4)$$

Thus we have divided the pixels into  $n$  groups, with the  $x$ - and  $y$ -displacement trajectories for each group of pixels described by linear functions of time. The choice of  $n$  involves a tradeoff between increased temporal resolution in the estimate of  $D$  for higher  $n$  and fewer parameters to estimate for lower  $n$ . Estimating fewer parameters reduces the chance of errors due to overfitting. For simplicity we consider here only cases where  $n$  is a divisor of  $wh$ , although removing this restriction is trivial.

Starting with an initial estimate  $p^0$  (see Section 3.5), we now derive the optimal change in parameters  $\Delta p$  in order to minimize  $E$ . Following Lucas and Kanade (1981) we perform a first-order Taylor expansion of the error function, centered at  $p^0$ .

$$E \approx \sum_t \left[ T(t, D(p^0)) + \nabla T \cdot \frac{\partial D}{\partial p} \cdot \Delta p - I(x(t), y(t)) \right]^2 \quad (5)$$

$T(t, D(p))$  denotes  $T$  sampled at position  $(x(t) + D_x(t), y(t) + D_y(t))$  with displacement  $D$  determined by the parameters  $p$ ,  $\nabla T$  is the (row vector) gradient of  $T$  at  $(x(t) + D_x(t), y(t) + D_y(t))$ , and  $\partial D/\partial p$  is the matrix of partial derivatives of the displacement at time  $t$  with respect to  $p$ , evaluated at  $p^0$ . For the parameterization of  $D$  described by Eq. (4), we have the partial derivatives:

$$\begin{aligned} \frac{\partial D_x(t)}{\partial p_k} &= \begin{cases} 1 - (t - t_k)/(\tau/n), & t_k < t < t_{k+1} \\ (t - t_k)/(\tau/n), & t_{k-1} < t < t_k \\ 0 & \text{otherwise} \end{cases} \\ \frac{\partial D_y(t)}{\partial p_k} &= \begin{cases} 1 - (t - t_{k-n-1})/(\tau/n), & t_{k-n-1} < t < t_{k-n} \\ (t - t_k)/(\tau/n), & t_{k-n-2} < t < t_{k-n-1} \\ 0 & \text{otherwise} \end{cases} \end{aligned} \quad (6)$$

To minimize  $E$  we differentiate Eq. (5) with respect to  $\Delta p$  and set the result equal to zero. Rearranging terms, we have

$$\begin{aligned} \sum_t (\nabla T \cdot \partial D/\partial p) \otimes (\nabla T \cdot \partial D/\partial p) \cdot \Delta p \\ = \sum_t (\nabla T \cdot \partial D/\partial p) \cdot (I(x(t), y(t)) - T(t, D(p_0))) \end{aligned} \quad (7)$$

where  $\otimes$  denotes a (matrix) outer product of row vectors ( $A \otimes B = \text{transpose}(A) \cdot B$ ). The quantity

$$H = \sum_t (\nabla T \cdot \partial D/\partial p) \otimes (\nabla T \cdot \partial D/\partial p) \quad (8)$$

is the Gauss–Newton approximation to the Hessian matrix of  $T(t, D(p))$  as function of  $p$ , evaluated at  $p^0$  (Baker and Matthews, 2004). We invert it to solve for  $\Delta p$ :

$$\Delta p = H^{-1} \cdot \sum_t (\nabla T \cdot \partial D/\partial p) \cdot (I(x(t), y(t)) - T(t, D(p))) \quad (9)$$

In theory  $H$  may be singular, meaning that minimization of  $E$  is an underdetermined problem and  $n$  is too large; however this never occurred during motion correction of any data from awake rats or in numerous simulations (see below).

Thus, we have determined the optimal change in displacement parameters in order to improve the match between the template and the distorted image.  $\Delta p$  is then added to  $p^0$  to yield  $p^1$ , and the process repeats. We denote the  $m$ th estimate of the  $k$ th parameter by  $p_k^m$ . The algorithm is also illustrated in a diagram (Supplementary Fig. 1).

### 3.4. Iterating to convergence

We wish to halt the repeating process of updating the displacement parameters  $p$  when the process converges to a final estimate of brain displacement in the image  $I$ . Since we cannot directly observe the difference between any of our successive estimations  $D(p^m)$  and the true trajectory of brain motion that occurred during a raster scan, instead we determine their accuracy by comparing the observed data image  $I$  to the displaced raster scan of the template  $T(t, D(p^m))$ . As in any gradient descent procedure, we must



**Table 1**  
Glossary of variables

$x, y$	Time-position functions
$\tau$	Frame duration
$t_{\text{pixel}}$	Duration of a single pixel in the raster scanned image
$w, h$	Frame dimensions
$I$	Image to be aligned to a template
$T$	Template
$D_x, D_y$	Time-displacement functions
$E$	Summed square error
$p$	Parameters
$k$	Parameter index
$m$	Iteration index
$n$	Number of parameterized positions, minus one; there are $2n + 2$ parameters total and $n$ linear segments in the estimated displacement trajectories
$\Delta p$	Parameter updates
$p^0$	Initial estimate
$H$	Pseudohessian matrix
$\Omega$	Correlation threshold for halting
$\beta$	Parameter update threshold for halting
$\Psi$	Correlation threshold for damping
$I_{\text{struct}}$	Structural component of an image
$I_{\text{var}}$	Fluorescence variation component of an image
$\sigma$	Noise amplitude
$q$	A point in the template $T$
$v_x, v_y, v'_x, v'_y$	Velocities
$F$	2D Fourier transform
$W$	2D cross-correlation evaluated at pixel coordinates
$D'$	Displacement mapping $T \rightarrow \mathbb{R}^2$

define a convergence criterion that specifies when further iterations are unlikely to improve the current estimate. Therefore we use a parameter update threshold  $\beta$  (in pixels or  $\mu\text{m}$ ), and halt when  $\max_k(|p_k^{m+1} - p_k^m|) < \beta$ .

In order to increase speed, and since our algorithm may be applied to imaging datasets in which only some frames show displacement artifacts, we also wish to halt whenever the match between  $I$  and  $T(t, D(p^m))$  is sufficiently good. A threshold for  $E$  is a poor choice for evaluating this match—since  $E$  is not normalized it is sensitive to the fluorescence gain factor which may change over time as the calcium indicator bleaches, is metabolized, or is sequestered into organelles; and since  $E$  is unbounded arbitrarily large errors may result from misalignment of only a few pixels or from small functional or noise-related changes in fluorescence. A better choice is to use the normalized and bounded standard Pearson correlation coefficient  $\rho$ , combined with thresholds on the parameter updates. Specifically, we define a correlation threshold for halting  $\Omega$  (unitless) and halt when  $\rho(I, T(t, D(p^m))) > \Omega$  or  $\max_k(|p_k^{m+1} - p_k^m|) < \beta$ . That is, we are halting when the estimated displacement gives a good match between the template and the displacement-distorted image, or when further iterations no longer change our solution. If speed is not paramount, or if displacements are expected to be large in each frame, the correlation threshold  $\Omega$  can be removed.

Once convergence is completed, we substitute the final estimate for  $p$  into Eq. (4) to determine the true position of each pixel. There is no guarantee that the final estimate represents the global optimum over all possible parameter values with respect to  $E$  or  $\rho$ , so accuracy must instead be confirmed by simulation and experiment (see below).

An additional optimization further improves the speed and accuracy of convergence. The first order Taylor approximation (5) of the square error (3) is imprecise for large values of  $\Delta p$  since  $T(t, D(p))$  is a nonlinear function of  $p$ . As a result, in some cases where  $p^m$  is already close to convergence the update  $\Delta p$  may repeatedly “overshoot” the minimum of  $E$ , causing oscillation in the values of  $p$ , and a delayed or even prevented convergence (Baker and Matthews, 2004). To solve this problem, we introduce a damping factor  $r$ , and

an additional correlation threshold  $\Psi$ . When  $\rho(I, T(t, D(p^m))) > \Psi$  and  $\rho(I, T(t, D(p^m))) \leq \rho(I, T(t, D(p^{m'})))$ , where  $m'$  is the iteration with the highest correlation so far, we set  $r = 1/(m - m')$ ; otherwise  $r = 1$ . Then  $p^{m+1} = p^m + \Delta p \cdot r$ . For two-photon calcium imaging of calcium indicator in awake rats, we used  $\Omega = 0.99$ ,  $\beta = 0.06$  pixels, and  $\Psi = 0.8$ . In the datasets considered below, convergence almost always occurred via  $\beta$ .

We classified a convergence as successful when  $\rho(I, T(t, D(p^m))) \geq 0.85$ . We chose 0.85 because this was the lower limit for correlation between frames that we observed in imaging data without motion artifacts. Note that this criterion is separate from  $\Omega = 0.99$ , the correlation threshold after which we no longer attempted to improve the displacement estimate further. We also classified displacement estimations as failed convergences when repeated iteration lead to displaced coordinates completely outside the boundaries of the template image for all pixels. For speed, we imposed a limit of 120 iterations; increasing this number did not affect the performance of the algorithm for any datasets or analyses, and this limit was rarely reached (see also Section 3.9).

### 3.5. Choosing an initial displacement estimate

We used three candidates for the initial estimate of displacement parameters  $p^0$ . First, the null displacement  $p^0 = 0$ , corresponding to a nondisplaced raster scan. Second, a constant displacement equal to the displacement  $D(\tau)$  detected at the end of the previous frame (waiting time between frames is  $< 0.5$  ms), corresponding to no additional displacement after the end of the previous frame. Third, the optimal full-frame translation to maximize cross-correlation between the template and the data (calculated via Fourier transform, see methods). Since all three methods require negligible computation compared to even a single iteration of the algorithm, we used all three. We first ordered them by the correlation value  $\rho(I, T(t, D(p^0)))$ , and then initiated iteration with each until converging to an estimate of  $p$  that gives  $\rho(I, T(t, D(p))) \geq 0.85$ , or until all three have been used.

### 3.6. Demonstration of displacement correction in silico

To illustrate the operation of our displacement correction procedure and to test its limits in detecting and correcting displacement, we performed computer simulations of two-photon imaging in awake animals. A raster scan pattern was passed over an image acquired *in vivo* and a known displacement trajectory was added, resulting in a distorted subimage. We then attempted to detect and correct the displacement using the algorithm detailed above. Note that while the solutions produced by our algorithm are linear interpolations of  $n + 1$  points and thus have temporal precision  $\tau/(n + 1) > t_{\text{pixel}}$ , the displacement trajectories introduced in these simulations were generated with temporal precision  $t_{\text{pixel}}$  and errors were evaluated on a pixel-by-pixel basis.

The procedure of distorting experimental data with artificial displacement, and subsequently correcting that displacement, is illustrated in Fig. 2. We used a two-photon image acquired under anesthesia from layer 2/3 of rat visual cortex, using green fluorescence from the cell-permeable calcium indicator Oregon Green BAPTA-1 AM-ester (OGB1-AM) and red fluorescence from the astrocyte marker SR-101 as described in previous work (Kerr et al., 2005). Visual inspection of the imaging sessions revealed no motion under anesthesia (spatial resolution  $0.8 \mu\text{m}/\text{pixel}$ ). The green-channel image (Fig. 2a, left) contains the somata of about 20 neurons and astrocytes, appearing as bright round shapes on a dimmer background; blood vessels appear as holes and fissures

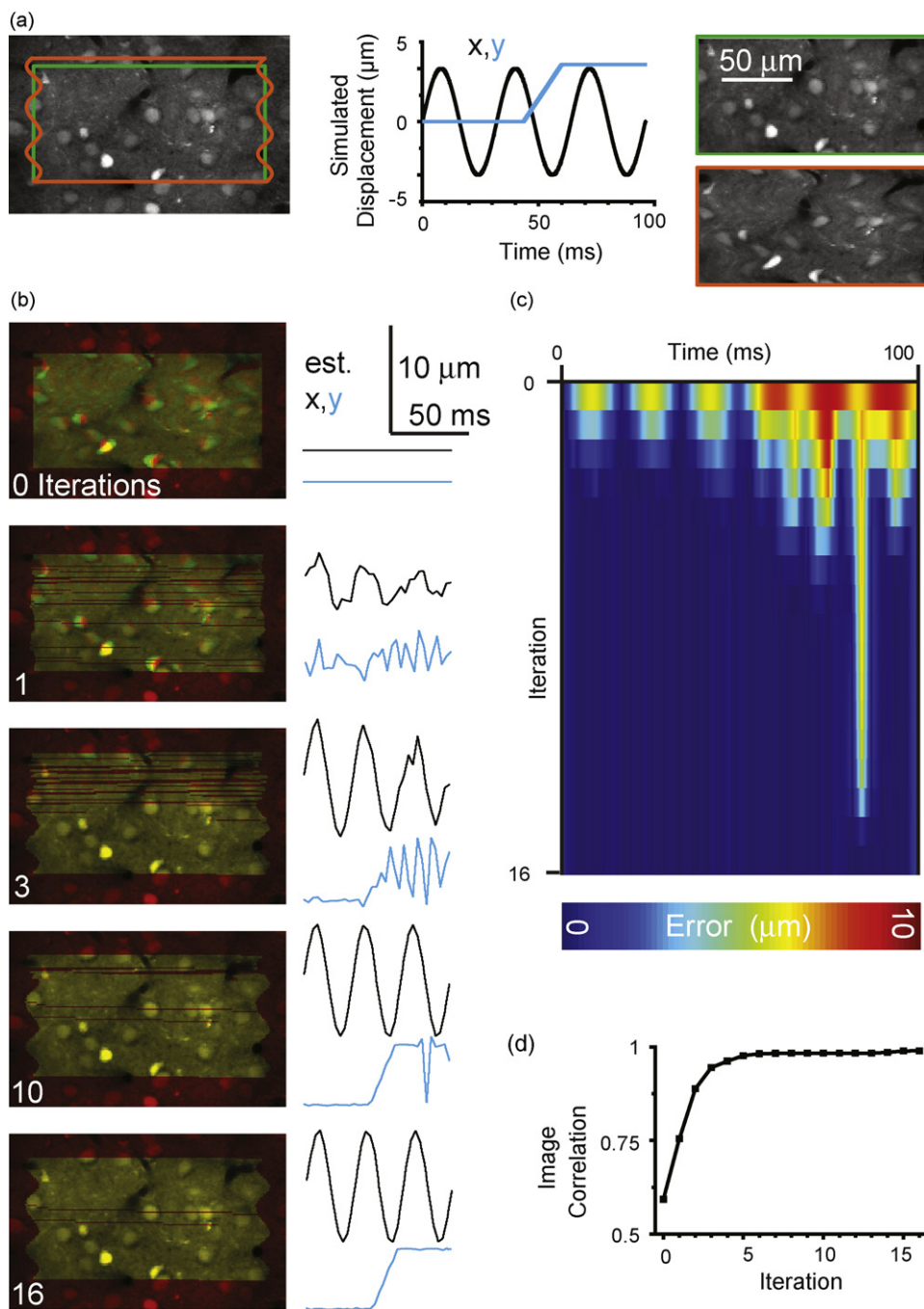


**Fig. 2.** Convergence to a correct estimate of within-frame displacement. (a) A raster scan was simulated by resampling an undistorted two-photon image from an anesthetized rat (left) using an undisturbed raster scan pattern (green rectangle) and a scan pattern disturbed by simulated motion of the specimen (orange shape). The simulated motion (center) consisted of sinusoidal displacement in the x direction ( $4\ \mu\text{m}$ , 3 cycles/frame or 31 Hz) and a single linear impulse in the y direction ( $4\ \mu\text{m}$ , 0.4 mm/s). The motion of the tissue leads to distortion of the resultant image as compared to the undisturbed raster scan (right). (b) A sequence of improving estimates of the displacement shown in panel (a) by the alignment algorithm, overlaid onto the original undistorted image. The distorted image before correction, as well as the 1st, 3rd, 10th, and 16th (final) iterative estimates are shown (left) alongside the estimated trajectory of x and y displacement within the frame (right). (c) Error in the estimated position of the excitation focus over the 96 ms raster scan for the uncorrected image and the sequence of 16 estimates. (d) Correlation of pixel fluorescence values in the displacement-distorted image with values from the corresponding pixels at the estimated (displaced) locations in the original undistorted image, shown as a function of iteration number.

darker than the background. Inspection of the red-channel image (not shown) allows discrimination of neurons (darker than background) and astrocytes (brighter than background).

Simulated raster scanning is demonstrated by passing a displacement-free raster scan pattern, consisting of 64 horizontal scan lines of 128 pixels each, over the region described by the green rectangle in Fig. 2a, left. We set spatial resolution to  $1.3\ \mu\text{m}/\text{pixel}$  and scan line duration to 1.5 ms (96 ms/frame), in order to simu-

late scanning conditions under which APs can be reliably detected from fluorescence signals *in vivo* (Kerr et al., 2005, 2007; Greenberg et al., 2008). This simulated scan results in an undistorted subimage (Fig. 2a, top right, green frame) consisting of the center of the original image.

Next, we applied displacement to the scan pattern. The displacement trajectory consisted of a sinusoid (3 cycles/frame,  $4\ \mu\text{m}$  amplitude) in the x direction and a single linear impulse (0.4 mm/s,

4  $\mu\text{m}$  amplitude) in the  $y$  direction (Fig. 2a, center). The resulting displaced scan pattern (Fig. 2a, left, orange contour) results in a distorted subimage (Fig. 2a, bottom right, orange frame). Using only the distorted subimage and the original undistorted template image, our procedure must estimate the displacement trajectory and assign each pixel to its true (displaced) position. We set  $n = 32$ , so that there were 256 pixels along each linear segment of the estimated displacement trajectories, and displacement was parameterized every 3 ms.

Prior to any iteration of the displacement estimation procedure, with  $p^0 = 0$  (see above), the observed data image (Fig. 2b, top left, green color) is not aligned to the template (red color). However, through subsequent iterations the estimated displacement parameters converge toward the true displacement applied in the simulation (Fig. 2b, right), and the image pixels move (Fig. 2b, left) to assume the true shape of the displaced raster scan (orange contour in Fig. 2a, left). Over successive iterations, the error in the estimation of the displacement trajectory tends toward zero for all time points (Fig. 2c). Correspondingly, the correlation  $\rho(I, T(t, D(p^m)))$  between template and data image tends toward 1 (Fig. 2d). Convergence via the parameter update threshold  $\beta$  was reached after 16 iterations. Note that the sudden linear impulse in the  $y$ -direction leaves two small gaps on the template to which no pixels are aligned (Fig. 2b, bottom).

### 3.7. Accuracy of displacement correction depends on multiple features of brain motion

We performed *in silico* tests using 3 types of displacement: continuous sinusoids, fast impulse displacements, and the displacement trajectories observed *in vivo*. For varying combinations of amplitude, frequency, and displacement angle we generated sinusoids of random phase and calculated the probability of convergence to a correct estimate as in Fig. 2. The results, averaged over all angles, are displayed as a 3D-surface plot (Fig. 3a, left). Convergence was near 100% for sinusoids 10  $\mu\text{m}$  or less in amplitude, and this limit did not depend on frequency for the range of 1–12 cycles/frame. For combinations of amplitude and frequency with 100% convergence for all angles, we calculated the root-mean-square error of the solutions (Fig. 3a, right). The estimated displacement was close to the true displacement ( $<2 \mu\text{m}$  in all cases, though usually much less), although displacements closer to the limit for 100% convergence produced larger errors.

We next examined linear impulse displacements of varying speed and amplitude, averaging over all angles and with random impulse latency (time from raster scan onset to displacement onset) (Fig. 3b, left). Convergence was near 100% for amplitudes up to about 7.5  $\mu\text{m}$ . Impulse velocity had a lesser effect on convergence, though for lower velocities ( $<1 \text{ mm/s}$ ) impulses of slightly greater amplitude were correctable. Combinations of amplitude and velocity with 100% convergence at all angles yielded estimates close to the true displacement trajectories ( $<0.75 \mu\text{m}$ , Fig. 3b, right).

We tested the effect of angle on the quality of displacement estimates. For displacement trajectories far from the convergence limit, angle had no effect (data not shown). We therefore deliberately chose displacement trajectories just on the boundary of what the method had proven capable of reliably correcting at all angles (green arrows in Fig. 3a and b; sinusoid 1 cycle/frame, 9.2  $\mu\text{m}$ ; impulse 5 mm/s, 7.36  $\mu\text{m}$ ). For these “hard” displacement trajectories estimation error showed a clear dependence on angle (Fig. 3c), with displacements in the  $y$  direction (across raster scan lines) generating more error than those in the  $x$  direction (along raster scan lines). The greater error for sinusoid displacement at all angles is irrelevant, since the velocity, frequency, and amplitudes were cho-

sen to illustrate the effect of angle on the two displacement types independently.

While it is informative to measure the limits of the displacement correction technique using simple displacements such as sinusoids and impulses, the true test of the method is whether it can estimate and correct the displacements ongoing in the brains of awake animals. To measure the method's capabilities using realistic displacement trajectories, we performed *in silico* tests using displacement detected *in vivo*. First, we applied our template-free displacement correction technique to two-photon imaging in awake rats ( $n = 6$  animals). After rejection of periods with axial displacements (7% of imaging data), the algorithm converged successfully for every imaging frame. Thus over our entire dataset of awake imaging sessions ( $n = 145,736$  frames,  $\tau = 96 \text{ ms}$ ), our algorithm has a 100% convergence rate.

Pooling together these displacement-corrected imaging sessions we compiled a library of displacement trajectories (e.g. Fig. 1c and d). We tested our algorithm's ability to correct these trajectories, drawing randomly from this library to displace raster scan patterns as in Fig. 2. We also multiplied the magnitude of the trajectories by a scaling factor ranging from 10% to 270% in increments of 10% to determine the effect on convergence and error rates (Fig. 3d). The alignment proved to be reliable with a convergence rate of 100% and mean error less than 0.1  $\mu\text{m}$  up to a scaling factor of 170%.

### 3.8. Generation of a displacement-free template image from distorted imaging frames

In the previous derivations and analyses, we considered the case of aligning a displacement-distorted imaging frame to an undistorted, displacement-free template image. Obtaining such a template should usually be possible at the end of an *in vivo* imaging session, but some experimental scenarios may prevent this. For example, the experimenter may wish to perform chronic imaging without anesthesia. It may also be necessary to perform on-line analysis of displacement-corrected fluorescence signals while the animal is still awake, with the result of the analysis directing the subsequent course of the experiment. The experiment may also end unexpectedly, such as with the sudden rupture of a blood vessel. A method to correct displacement without collecting a displacement-free template is therefore desirable.

We describe such method to generate a stable template automatically from a sequence of motion-distorted imaging frames (see Appendix A), requiring only a modest minimum recording duration, and that a single assumption about the experiment is met. Specifically, we require that over many successive imaging frames the mean velocity of the imaged tissue measured at any fixed time  $t$  after the start of each raster scan will be zero. Since the motion of the brain in the awake animal lacks any causal relation to when, for what duration, and how often our raster scans take place, and since the brain of a head-fixed animal does not move large distances over time, this assumption holds true in almost every conceivable experiment: the mean velocity for any  $t$  will approach zero as the number of imaging frames increases. The only exception might be when the experimenter deliberately synchronizes the start of a raster scan to some biological event related to brain movement, such as heartbeat, respiration, or motor activity. For the purposes of displacement correction, continuous imaging is recommended instead. When synchronization of raster scanning to movement related events is essential to an experiment, a few additional minutes of unsynchronized imaging can provide a displacement-free template, to which the synchronized imaging can then be aligned.

We tested the performance of motion correction with automatic template generation *in silico* using a base image from an anesthetized animal (Supplementary Fig. 2a). However, while the



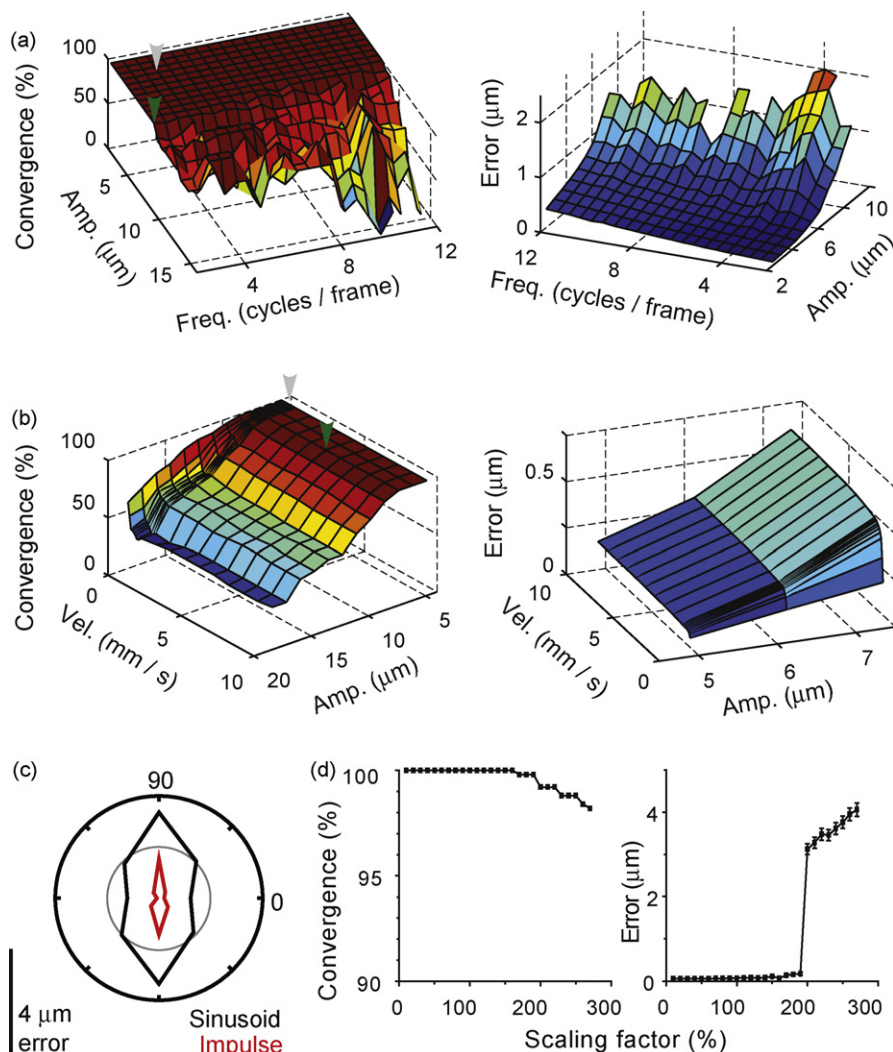


**Fig. 3.** Performance limits of the alignment algorithm. (a) Convergence of the alignment algorithm as a function of frequency and amplitude of sinusoidal displacement (left). Data shown is an average over all displacement angles. Average estimation error as a function of sinusoid noise and amplitude (right), for the frequency/amplitude combinations yielding 100% convergence. Gray arrow indicates x-displacement used in Fig. 2, green arrow corresponds to panel (c). (b) Convergence (left) and estimation error (right) as a function of velocity and amplitude for linear impulse displacements. Gray arrow indicates y-displacement used in Fig. 2, green arrow corresponds to panel (c). (c) Estimation error as a function of displacement angle for sinusoidal (black, 1 cycle/frame, 9.2  $\mu\text{m}$  amplitude) and impulse (red, 5 mm/s, 7.36  $\mu\text{m}$  amplitude) displacements. (d) Convergence (left) and estimation error (right) in correction of simulated displacement using displacement trajectories observed in awake rats ( $n=6$ ). Error bars indicate standard error of the mean. The x-axis shows the scaling factor by which the magnitude of the detected displacement was multiplied before being used to disturb the raster scan position.

base image was resampled by a sequence of displaced raster scan patterns to generate distorted frames, it was not used as a template for the displacement correction. Instead, the distorted frames were the only source of information provided to the algorithm, which performed increasingly well at estimating both single-frame displacement (Supplementary Fig. 2a, center) and an undistorted average image (Supplementary Fig. 2a, right) as greater numbers of frames were provided. The displacement estimation error fell to almost zero after 30 frames, and remained low thereafter when tested using up to 500 frames (Supplementary Fig. 2b). Since this procedure estimated the displaced positions of imaging frames that do not overlap completely, it produced average images larger than any individual imaging frame (for details, see Appendix A).

### 3.9. The effect of “noise”

We next examined how the accuracy of motion correction depends on the magnitude of fluorescence variations unrelated to displacement. These variations can originate from multiple sources,

including AP discharge in neurons, presynaptic activity in the neuropil background (Kerr et al., 2005), detector shot noise, digitization noise, z-movements below the axial resolution limit, calcium release due to backpropagation of APs into dendrites, as well as other unanticipated sources. Depending on the experiment, these sources of variation might be considered either signal or noise, but in any case they are unrelated to displacement. To our knowledge, no study to date has provided a comprehensive description of signal- and noise-related fluorescence variations for *in vivo* imaging of bulk-loaded calcium indicator. While such a description is well beyond the scope of the present work, it is nonetheless desirable to determine the effect of realistic fluorescence variations on motion correction accuracy.

We therefore developed a simple data-centric method to manipulate the magnitude of realistic fluorescence variations *in silico* that did not rely on an explicit model of fluorescence variations. We began with a sequence of imaging frames  $I$  collected from an anesthetized animal displaying no displacement, and calculated the average image  $T = \langle I \rangle$  (Fig. 4a). Next, we decomposed each image



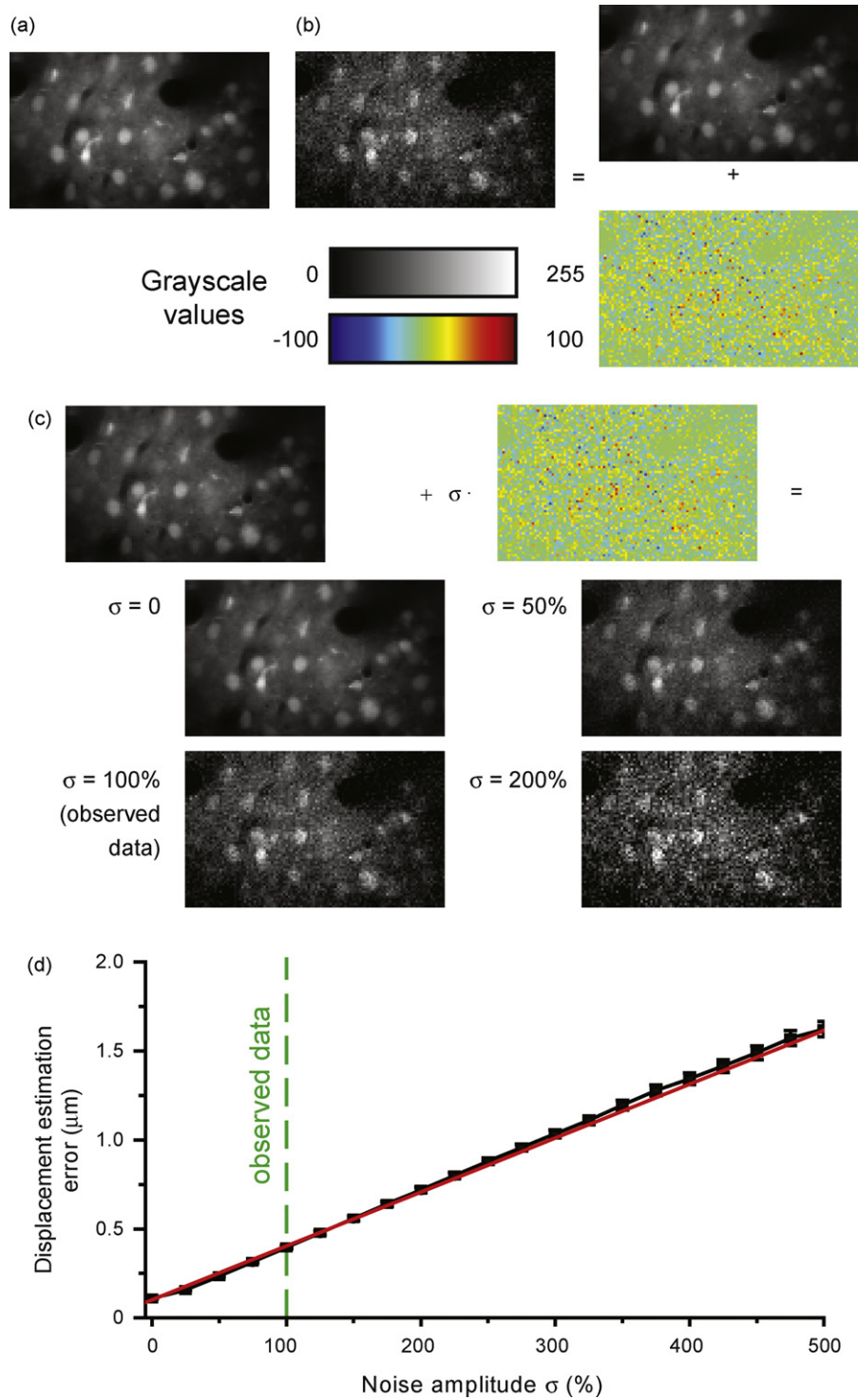


**Fig. 4.** The effect of fluorescence variation on displacement estimation accuracy (a) Average image from an imaging session in an anesthetized rat that displayed no motion artifacts. (b) Single frame (left) contributing to the average in (a), and decomposition of the frame into structural (upper right) and fluorescence variation components (lower right). (c) Reconstruction of the frame shown in (b) with the fluorescence variation component adjusted by a scaling factor  $\sigma$ , termed the “noise amplitude.” Results are shown for  $\sigma = 0$ , 50%, 100%, and 200%. (d) Mean displacement estimation error as a function of noise amplitude. Error bars indicate s.e.m., red line shows regression, dashed green line indicates  $\sigma = 100\%$ , corresponding to the imaging data in awake animals.

by a linear projection into a structural component totally correlated to  $T$  and a fluorescence variation component orthogonal (i.e. totally uncorrelated) to  $T$  (Fig. 4b):

$$I_{\text{struct}} = \frac{I \cdot T}{T \cdot T} T, \quad I_{\text{var}} = I - I_{\text{struct}} \quad (10)$$

where the dot products are taken over all image pixels. We then reconstructed the individual images by adding the structural component to a scaled version of the fluorescence variation component:

$$I(\sigma) = I_{\text{struct}} + \sigma I_{\text{var}} \quad (11)$$

The scaling ratio  $\sigma$ , which we term the “noise amplitude,” determines the amount of fluorescence variation in the reconstructed images.  $\sigma = 0$  yields images totally correlated with the average  $T$ , while  $\sigma = 100\%$  reproduces the original data (Fig. 4c). We next used unaltered displacement trajectories from awake rats to perturb the reconstructed images  $\hat{I}(\sigma)$ , and attempted to align the distorted images to  $T$  as described above (Fig. 2). We measured displacement estimation error as a function of noise amplitude, varying  $\sigma$  in increments of 25% from 0 to 500% (Fig. 4d). Mean error remained low ( $0.4\ \mu\text{m}$ ) for realistic fluorescence variations ( $\sigma = 100\%$ ), was less than  $1\ \mu\text{m}$  for all  $\sigma < 300\%$  ( $n = 500$  frames), and showed a tight linear association with  $\sigma$ . A linear regression indicated that increasing noise amplitude by 10% of the size observed *in vivo* increased displacement estimation error by  $0.03\ \mu\text{m}$ . For this analysis we did not require a final correlation value of 0.85 between image and template, since we were intentionally manipulating this correlation by adjusting  $\sigma$ . However, all frames did converge successfully via the parameter update threshold  $\beta$ , even for  $\sigma = 500\%$ . Calculating the fluorescence variation component by subtracting the average instead of subtracting the structural component yielded much lower errors (data not shown).

### 3.10. Two channel imaging confirms accurate displacement correction *in vivo* and allows motion correction of noisy or feature-poor data

The scaling limit of 170% for correction of realistic displacement trajectories and the small errors associated with realistic fluorescence noise suggest that when faced with the brain displacements typical in awake rats, our algorithm's estimates are likely to be accurate. Even at larger scaling ratios or noise amplitudes estimation errors remained small (e.g.  $0.57\ \mu\text{m}$  at 190% scaling and  $1\ \mu\text{m}$  at 300% noise). The fact that all three types of *in silico* tests showed small or nonexistent estimation errors when convergence approached 100%, along with the 100% convergence observed for displacement estimation in imaging of awake animals, suggests that estimates of *in vivo* displacement were nearly error-free. While these findings are encouraging, they do not totally exclude the possibility of serious errors *in vivo*. Erroneous correction of displacements in awake animals might result in incorrect displacement estimates that are themselves correctable in simulations, leading to lower errors *in silico* than *in vivo*. We therefore introduce two additional tests to show that displacement estimation errors for *in vivo* data are small.

First, we inspected the corrected imaging visually. After estimating displacement in an imaging frame each pixel was corrected to its appropriate position. We also inverted the displacement functions to map regions of interest (ROIs) in the template image  $T$  back onto individual distorted frames, allowing ROI tracking in the original raw image frames  $I$ . Visual inspection reveals that image features such as somata and blood vessels do not move or change shape in the corrected imaging (Supplementary Movie 3), while in the uncorrected imaging (Supplementary Movie 1) they can be accurately tracked by ROIs which move and change shape automatically according to the estimated displacement (Supplementary Movie 2). While somewhat subjective, this result shows that errors in displacement estimation are at least too small to be visibly discerned.

For a more quantitative confirmation, we obtained two-channel images via simultaneous excitation of two different fluorophores in an awake, head retrained animal, and compared the resulting displacement estimations. Green fluorescence from bulk loaded OGB1 and red fluorescence from SR-101 were separated using dichroic filters, forming two separate images for each raster scan (Fig. 5a). Note that the fluorescence from the calcium sensitive dye OGB1 is a functional signal originating from neurons, astrocytes,

and the background neuropil, while SR-101 fluorescence provides only structural information by staining astrocytes. Displacement estimation (with automatic template generation) proceeded as described above, yielding trajectories for each image frame (Fig. 5c). Visual inspection showed that corrected frames took on similar shapes (Supplementary Fig. 5b). The probability distribution of the discrepancy between the two displacement estimations peaked at zero, and dropped off rapidly for discrepancies  $>1$  pixel (Fig. 5d; mean  $x$ -discrepancy was  $<1$  pixel =  $1.6\ \mu\text{m}$  for 99.6% of imaging frames,  $y$ -discrepancy 97.8%, total discrepancy 96.7%;  $n = 3$  animals, 4500 frames). We emphasize that this confirmation involved no simulations of displacement; instead both image channels consisted of raw *in vivo* imaging data and were collected simultaneously. Therefore, both channels contained all noise sources present in fluorescent measurements of awake animals.

Our algorithm for displacement correction depends on matching features between individual images. Consequently, we can expect it to fail when fluorescence amplitude is uniform over large regions of an image that cover its entire horizontal span. To test this we used an imaging session in an anesthetized animal that (exceptionally) contained ongoing low-amplitude displacement, in which a red channel contained fluorescence from SR101 and a green channel contained fluorescence from a single neuron filled with OGB1 intracellularly. We performed motion correction (again with automatic template generation) on both image channels and compared the results. The green channel, whose fluorescence was restricted to a single neuron's soma and a horizontal patch pipette in the center of the frame, produced displacement trajectories with large fluctuations and distorted the imaging frames (Fig. 5e; displacement estimated based on green channel with resulting correction applied to both red and green channels). The red channel, which contained fluorescence from several astrocytes which spread their fine processes across the frame to envelop (unseen) neurons and blood vessels, produced undistorted images that closely resembled raw image frames except for correcting the low-amplitude displacements (Fig. 5f). Using the displacement estimates generated by motion-correcting the red channel, we were able to extract from the green channel the AP-associated calcium transients elicited by a series of current pulse injections (Fig. 5g). In contrast, using the displacement estimates generated by motion-correcting the green channel caused calcium transients to be masked by motion artifacts, and the baseline fluorescence of the neuron to decrease. We conclude from this analysis that an image channel too noisy or lacking in contrast for displacement estimation can be successfully motion corrected by combining it with a second structural channel.

### 3.11. Statistical description of brain motion

Together, the various *in silico* tests, the visual inspection of corrected imaging, and the close agreement of displacement estimations from different bulk-loaded fluorophores all support the accuracy of the displacement estimation procedure in awake animals. Consequently, the results of displacement estimation describe the motion occurring in the brains of awake head-fixed rats. While we have approached this motion mainly as a problem to be overcome, it is also an interesting result in its own light, which we report in Supplementary Fig. 3. Summarizing briefly, we note that (1) distributions of velocity and frame-wide displacement range differed among animals in both mean and shape; (2) most animals showed a  $>50\%$  chance of ongoing motion every 4 ms; (3) all animals showed a  $>50\%$  chance of ongoing motion every 96 ms; (4) average velocity along the rostro-caudal axis was always greater than along the medio-lateral axis, although the two showed a strong linear relation over the 6 animals; and (5) both rostro-

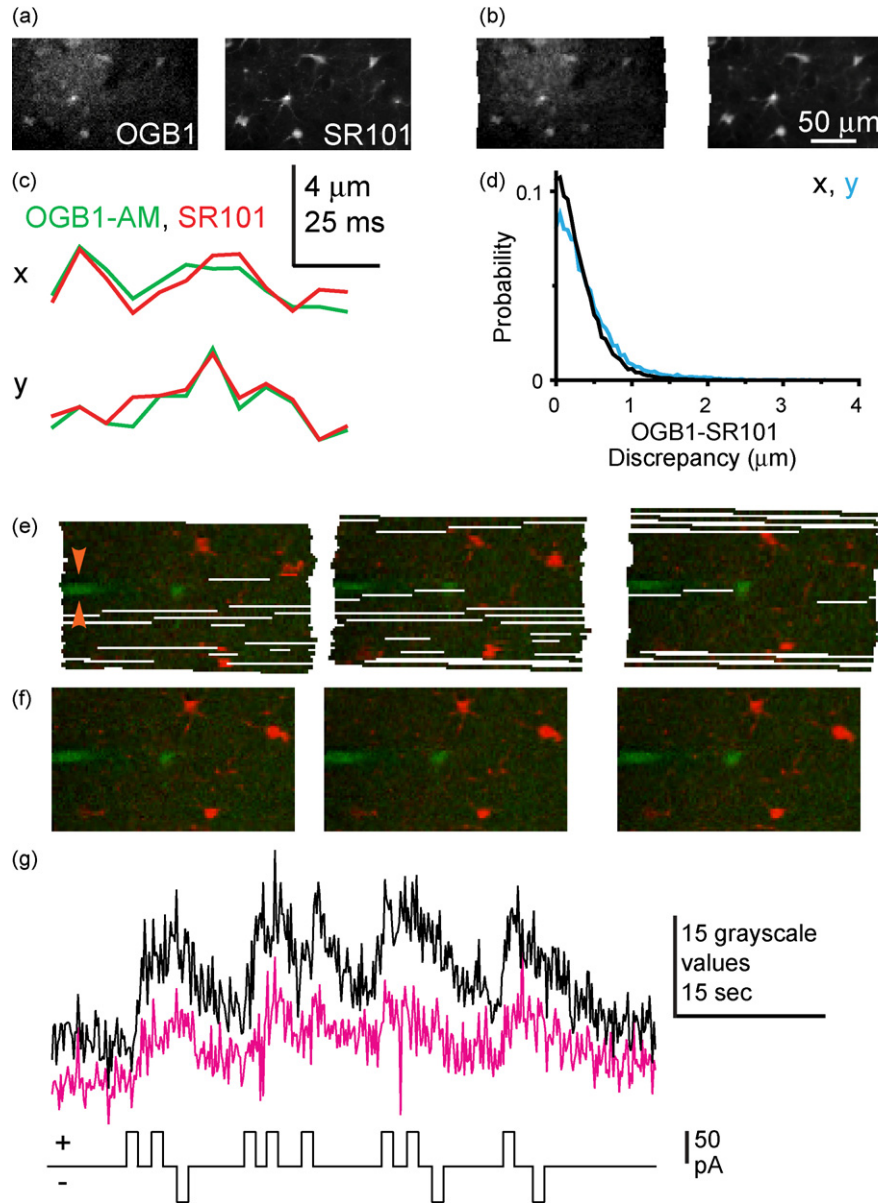


**Fig. 5.** Alignment based on independent image channels (a) Images of the same brain region acquired simultaneously in an awake rat by separating green light from OGB-1 fluorescence and red light from SR101 fluorescence using a dichroic filter. (b) Images from (a) after displacement correction, performed on each data channel independently. (c) Estimated  $x$ - and  $y$ -displacement for the frames shown in (a) and (b). (d) Probability distribution of the discrepancy between estimated displacement using OGB1 vs. SR101 fluorescence ( $n = 3$  animals, 4500 frames). (e) As in (b), but with OGB1 loaded into a single neuron intracellularly instead of bulk-loaded into all local neurons. Three successive imaging frames are shown; the recording pipette appears as a fluorescent horizontal stripe across the left side of the image (orange arrows). Displacement estimates generated from the green channel were used to correct both green and red channels. (f) Displacement estimates generated from the red channel used to correct both green and red channels; same frames as (e). (g) Neuronal fluorescence signal (upper) collected from the green channel using displacement estimates generated from the green channel (purple) or the red channel (black). Imaging proceeded with simultaneous current injection (lower).

caudal and medio-lateral displacement within single frames rarely exceeded 10 μm.

### 3.12. Computational cost of the algorithm

We next investigated theoretically and empirically how the computation required for displacement correction scaled with the amount of brain motion, the image size, and temporal precision of the displacement estimation. The number of iterations required before convergence is data-dependent, while the time per iteration is not. For the general case of the Lucas–Kanade algorithm, iteratively updating the parameter estimates to determine  $p^{m+1}$  from  $p^m$  requires  $O(n^2hw + n^3)$  operations, with the most costly steps

being calculation of the Hessian matrix with  $O(n^2hw)$  operations and inverting it with  $O(n^3)$  operations (Baker and Matthews, 2004).

However, in the present case we can take considerable advantage of our particular parameterization to decrease computational complexity. Note that for each pixel time  $t$ , the row vector  $\nabla T \cdot \partial D / \partial p$  has only 4 nonzero elements out of  $(2n + 2)$  total elements, so the summand used to calculate  $H$  in Eq. (8) has only 16 nonzero elements out of  $(n^2 + 8n + 4)$  total elements. Therefore calculating the summand in Eq. (8) has complexity  $O(1)$ , and calculating  $H$  by summing over  $t$  requires modifying 16 of its elements  $hw$  times with complexity  $O(hw)$ . Overall,  $H$  has  $(12n + 4)$  nonzero elements, so it can be inverted by Gaussian elimination in  $O(n^2)$  operations. All other operations (such as calculating  $T$ ,  $\nabla T$ ,  $\nabla T \cdot \partial D / \partial p$ , etc.) require



$O(hw)$  operations, with the exception of multiplying by  $H^{-1}$  to solve for  $\Delta p$  which requires  $O(n^2)$ . Thus our overall computational complexity is  $O(hw + n^2)$ . We exploited this fact by updating only those values of  $H$  and  $\nabla T \cdot \partial D / \partial p$  capable of being nonzero to increase the iteration speed.

In practice, we found no dependence of computation time per iteration on  $n$  for values ranging from 1 to 64, with computation time remaining about 10 ms per iteration for a  $64 \times 128$  imaging frame (Supplementary Fig. 4a, including memory initialization and other overhead computations). Fixing  $n = 16$ , we also found that the average number of iterations required to correct displacement trajectories from awake rats increased linearly with the scaling factor (Supplementary Fig. 4b), requiring 5.28 iterations for a scaling factor of 25%, 5.81 for 100%, and 29.78 for 1000%. For  $n = 16$ , displacement correction of  $64 \times 128$  imaging in awake rats usually required 50–100 ms/frame overall (2.99 GHz processor). We also performed displacement correction for a single 1200 frame sequence of  $128 \times 128$  imaging in an awake rat showing low-amplitude motion artifacts in 3.62, 2.56, and 1.95 min for  $n = 128$ , 64, and 32 (18, 13, and 9.5 ms/frame).

A considerable portion of computation time (about 10%) consisted of calculating optimal full-frame translations via Fourier transform prior to any iterative steps (see Section 2). Since all motion correction operations were performed in Matlab, we expect that speed could be further increased by using a compiled language. Also, since alignment of each imaging frame to the template can proceed independently, our algorithm could be run in parallel on multiple processors or computers.

### 3.13. Displacement correction allows accurate detection of AP times from functional fluorescent signals

As a further test of the practical application of our displacement correction method, we examined the effects of corrected and uncorrected displacement on the detection of AP times from fluorescence signals. The occurrence of an AP causes voltage gated calcium channels to open, thereby increasing the intracellular calcium concentration. Observation of calcium indicator fluorescence can therefore be used to determine the times of AP-evoked fluorescence transients (Kerr et al., 2005, 2007) and to determine the number APs giving rise to each transient (Greenberg et al., 2008).

We analyzed imaging sessions with simultaneous cell-attached electrical recordings of neurons (Fig. 6a). In these data sets, APs detected electrically were accompanied by sharp upward deflections in the fluorescence originating from an ROI enclosing the soma of the electrically recorded neuron, followed by exponential decay back to baseline fluorescence levels (Fig. 6b). Performing *in silico* raster scan displacements using sinusoid or impulse trajectories, or those from the library of awake-animal trajectories described above, caused the fluorescence signals to become distorted and unusable (Fig. 6c, left). This is because the neuron's soma will be constantly entering and exiting any fixed ROI enclosing its soma. This problem cannot be alleviated by using a larger ROI including the soma together with the surrounding neuropil background, as this would corrupt the desired signals with the strong time-varying background fluorescence previously observed with OGB1-AM *in vivo* (the Optical Encephalogram, or OEG) (Kerr and Denk, 2008; Kerr et al., 2005). Estimation and correction of displacement allows recovery of the desired fluorescence signals, either by correcting the displacement in each image frame (Supplementary Movie 3) and applying a stationary ROI, or by using the estimated displacement to track the neuron's somata with a moving ROI (see Supplementary Movie 2). We calculated kinetics by correcting the

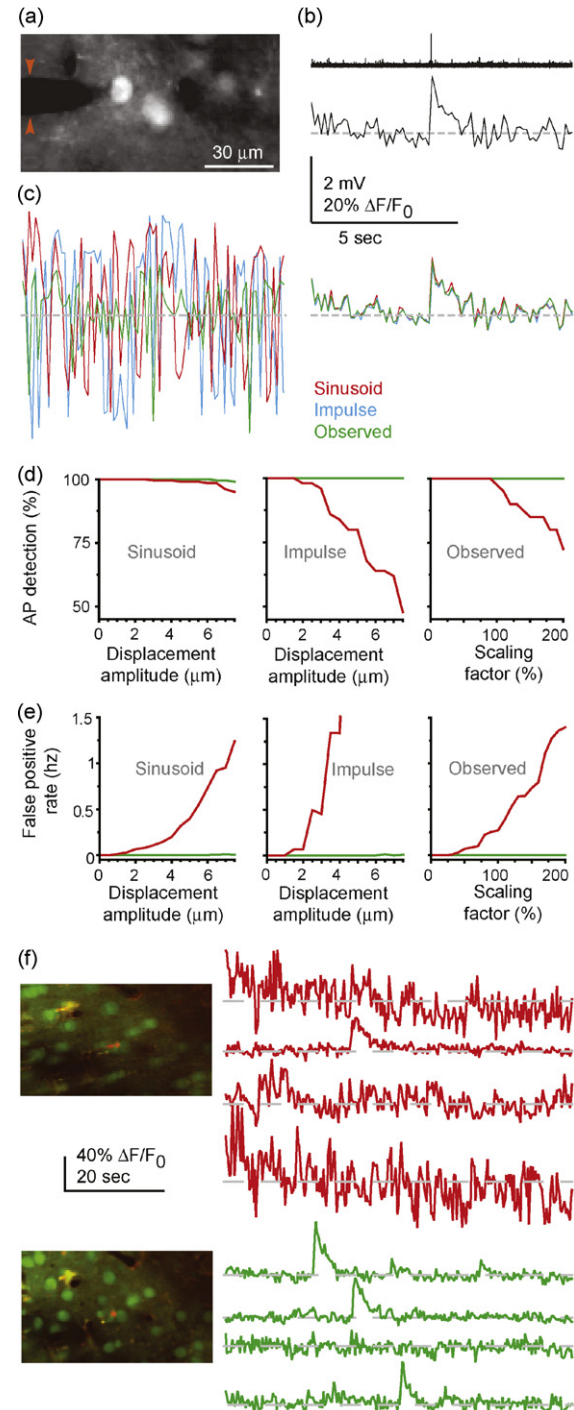


**Fig. 6.** Alignment allows recovery of functional signals (a) Two-photon image taken during cell-attached recording in an anesthetized rat. The recording pipette appears as a horizontal shadow across the left side of the image (orange arrows). (b) 10 s of voltage measurements from cell-attached recording shown in (a) (top), with one action potential. Simultaneously detected OGB1-AM fluorescence averaged across the soma of the electrically recorded neuron for each 96 ms frame (bottom, dashed line indicates baseline). (c) Frame-averaged OGB1-AM fluorescence as in (b) (left) after disturbing each frame's raster scan with a sinusoid (red, 1 cycle/frame,  $6 \mu\text{m}$ ), a linear impulse (cyan, 1 mm/s,  $6 \mu\text{m}$ ), or displacement trajectories observed *in vivo* (green). Frame averaged fluorescence after correcting for displacement using the alignment algorithm (right). (d) Chance of detecting an action potential via fluorescence signals for uncorrected (red) and corrected (green) displacements of increasing amplitude. (e) Rate of false positives in action potential detection for uncorrected (red) and corrected (green) displacements of increasing amplitude. (f) Uncorrected average image (top left) and fluorescence signals from four neuronal somata (top right) in a population bulk-loaded loaded with OGB1-AM. Corrected average (bottom left) and neuronal fluorescence signals (bottom right).



displacement in each image frame, and then performing a normalization to correct for ROI pixels that were absent due to gaps in the scan pattern caused by displacement or due to being displaced outside the image frame (see Section 2). For all three displacement types considered, the corrected fluorescence signals resemble each other as well as the original fluorescence transient (Fig. 6c, right). Employing an automated procedure for spike detection described in previous work (Greenberg et al., 2008) we found that as displacement amplitude increased, uncorrected imaging showed a decreased rate of AP detection (Fig. 6d, red traces) and an increased rate of false positives (putative APs inferred when no AP actually occurred, Fig. 6e, red traces). Corrected imaging, however, continued to detect APs without generating false positives (Fig. 6d and e, green traces). When applied to imaging of larger populations in awake animals, motion correction produced stable average images and neuronal fluorescence signals with AP transients and a stable baseline, whereas uncorrected imaging yielded a blurred average and corrupted fluorescence signals (Fig. 6f).

We conclude from these analyses that for sinusoidal and impulse displacements greater than 1  $\mu\text{m}$ , and for realistic displacement trajectories at least 40% as large as those occurring in awake head-fixed rats, displacement correction is required for accurate AP detection. Note that while displacements were added *in silico*, a sequence of image frames containing an AP-associated transient consisted of raw data from *in vivo* experiments, and therefore contained spatiotemporal fluorescence variations unrelated to motion.

### 3.14. Demonstration on additional datasets

Finally, we examined the applicability of our algorithm to two other types of two-photon imaging data that may arise in neuroscience research, and confirmed successful alignment by visual inspection of ROI tracking. The first imaging dataset showed a population of neurons bulk-loaded with calcium indicator and imaged at low zoom to maximize the field of view, with a spatial resolution of 2.3  $\mu\text{m}/\text{pixel}$  (Supplementary Movie 4). After motion correction with automatic template generation, visual inspection showed that ROIs corresponding to 45 neurons (red) and a blood vessel (green) were successfully tracked during brain tissue motion. The second imaging showed a dendrite in the cortex of a mouse loaded with Cyan Fluorescent Protein (CFP), imaged at high zoom to resolve fine structure, with spatial resolution 0.2  $\mu\text{m}/\text{pixel}$  (Supplementary Movie 5). Motion correction with automatic template generation allowed successful tracking of ROIs corresponding to a segment of dendrite (green) and several dendritic spines (red).

## 4. Discussion

Our results demonstrate that displacement artifacts arising during two-photon imaging of awake animals can be corrected by a fully automated procedure. Furthermore, this procedure requires only a single channel of imaging data with no other data provided, does not require collection of a displacement-free template image, and makes no assumptions about the form of displacement to be corrected. The procedure performs well on a wide variety of displacement trajectories, but was specifically designed for and tested on the displacements ongoing in the brains of awake head-fixed rats.

In addition to demonstrating the method's success in detecting and correcting several different types of displacement trajectories, *in silico* alignment tests suggested that the convergence rates near 100% observed *in vivo* are indicative of accurate displacement estimation. This was born out both by visual inspection of the cor-

rected imaging and by quantitative comparison of displacement estimates derived from different image channels. While we might have also tested limitless other displacement trajectory types *in silico*, we elected to halt at three types for brevity and simplicity. The sinusoids and impulses indicated the technique's limits, while the library of displacement trajectories detected in awake animals provide a sense of its performance in practice. We also showed that the displacement estimation errors resulting from realistic signal- and noise-based variations in fluorescence *in vivo* are small.

Using a piecewise linear basis was perhaps the simplest parameterization of displacement imaginable. No major changes to the computations discussed above would be required for any other linear basis, such as sinusoids, wavelets, square waves, etc. For nonlinear differentiable parameterizations such as splines, the feasibility of calculating  $\partial D/\partial p$  would have to be examined on a case-by-case basis.

While we defined successful alignment for *in silico* tests by a correlation threshold of 0.85, this threshold can be omitted and is intended only as a guideline for interpreting the results of motion correction; in general the appropriate threshold will depend on the type and quality of data. It is ultimately up to the experimenter to decide what a sufficiently good match is once the parameter updates  $\Delta p$  tend toward zero, possibly with reference to some experimental confirmation such as our comparison of OGB1 and SR101 signals. If it is expected that some imaging frames may be corrupted by factors unrelated to displacement, another (lower) correlation threshold can be used to select frames in which estimation of displacement and alignment to the template were successful. While we manually excluded imaging epochs with z-shifts, we also found that a correlation threshold of 0.85 could also be used to automatically separate frames with different z-shifts while aligning those with similar z-shifts (data not shown).

Disk space considerations may arise when storing corrected imaging data. The most efficient storage option is of course simply to store the displacement parameters  $p$ , but this may make further analysis of imaging data time-consuming to execute and cumbersome to program. The other extreme is storing the displaced  $x$ - and  $y$ -positions of every pixel in every frame, but this yields an array twice as large as the imaging data itself, and probably with more bytes/sample since many imaging programs digitize fluorescence to only 8 bits. A happy medium may be to select ROIs in the displacement corrected average and to store the corrected position of these ROIs' pixels in each uncorrected frame as calculated through  $D^{-1}$ ; this solution requires a large initial computation but relatively little storage and calculation thereafter.

Interestingly, we found that more movement occurred on the rostro-caudal axis than the medio-lateral (Supplementary Fig. 4c), as reported previously for awake head-fixed mice (Dombeck et al., 2007). Since movement along the scan lines proved easier to correct than movement across scan lines (Fig. 3c), motion correction might be improved at no cost simply by running scan lines across the rostro-caudal axis.

Another motion correction technique using a Hidden Markov Model (HMM) has been applied to imaging data from head-fixed mice running on a sphere (Dombeck et al., 2007). Unlike the algorithm presented here, which estimates displacement trajectories as piecewise linear functions, the HMM estimates  $x$ - and  $y$ -displacement trajectories as step functions. A major advantage of the HMM approach over the gradient descent approach taken here is that the HMM is guaranteed to find the globally optimal trajectory among all allowed trajectories, whereas the algorithm presented here can reach local minima in its error function.

The method presented here also possesses several advantages. Its solutions can reach subpixel accuracy (Figs. 2–5) with no maximum displacement. Its current solutions are piecewise linear,

allowing perfect fits for constant velocities and stretched or non-horizontal scan lines where needed (e.g. Fig. 2b). Extending it to use any (e.g. sinusoidal) basis for interpolation would be trivial to implement (though perhaps computationally costly for non-sparse H). It requires no prior assumptions about the distribution of displacement trajectories, allowing it to be applied to all animals despite variation in displacement distribution shape and spatial asymmetry (Supplementary Fig. 4). It can generate a displacement-free average from distorted images and aligns all pixels in each frame to produce an average image larger than the individual images.

We observed large maximum displacements within single frames, in some cases  $>10\ \mu\text{m}$  (e.g. Fig. 1), using head-fixed rats 28–32 days old. Whether this movement becomes greater in a freely moving animals still needs to be tested using head-mounted fiber optic microscopes (Helmchen et al., 2001; Sawinski and Denk, 2007).

While we have focused here on two-photon imaging, our method is equally applicable to any imaging technique which acquires pixel intensity values nonsynchronously. This includes confocal microscopy (Minsky, 1961),  $4\pi$  microscopy (Hell and Stelzer, 1992), and second harmonic generation (Freund and Deutsch, 1986) for which no modification of the above procedures is required. Our algorithm might also be adapted to functional magnetic resonance imaging if the relationship between physical displacement trajectories and displacement of  $k$ -space trajectories could be determined.

Several future directions would be worth pursuing for this method. Incorporating nonrectangular scan patterns such as two- or three-dimensional curves is mathematically trivial, and automatic template generation in 3D could make use of imaging periods with constant  $z$ -shifts. Convergence, error, and speed might be improved by seeding an initial estimate using lower temporal resolution, an HMM, or optimal translations for smaller parts of the frame. Displacement estimation could be optimized with respect to a model of fluorescence noise using a weighted error function (Baker and Matthews, 2004) although a realistic model would require detailed investigation of the complex spatiotemporal correlations of *in vivo* fluorescence noise. Additional error terms could also be introduced to impose a prior on displacement trajectories (Baker and Matthews, 2004). Template-less correction of long imaging sessions combined with spatial filtering (Broser et al., 2004) and compensation for optical aberration (Feierabend et al., 2004) might allow a “super-resolution” average showing increased spatial detail. While technically challenging, online motion correction in real time with automatic compensatory movements could quickly correct  $z$ -shifts, reduce the effective size of sudden lateral shifts, stabilize electrode position while recording from neurons or dendrites in awake animals, and ensure accurate optical control of neuronal activity (Gradinaru et al., 2007). These developments promise to further increase access to biological systems in awake animals, and we invite contact from research groups wishing to apply our method to these and other datasets.

## Acknowledgments

We thank Arthur Houweling for training animals for head-fixation, Damian Wallace and Mazahir Hasan for a segment of imaging of a CFP-labeled dendrite, Arno Schmitt for a segment of imaging with SR101 and intracellularly filled OGB1, Winfried Denk and Bert Sakmann for encouragement and generous support, and Kevin Briggman for comments on an earlier version of this manuscript. Supported by the Max Planck Society.

## Appendix A. Displacement estimation without a displacement-free template image

First, choose a frame from an imaging session, either by visual inspection, minimum absolute difference from the previous frame, or randomly. Next, use this frame as a template  $T$  for displacement estimation, aligning as many other frames to it as will successfully converge (as in Fig. 2 and Supplementary Fig. 1). However, since the template itself is distorted, the displacement estimates are valued in units of pixels of  $T$ , as opposed to units of the desired pixel positions in the target brain structure. For a given frame  $I$  we then have a composition of two coordinate changes: the just-estimated displacement  $D$  mapping from the coordinates of the distorted image  $I$  to the coordinates of the distorted template  $T$ , and some unknown displacement mapping  $D'$  from the coordinates of  $T$  into a plane of physical reality  $\mathbb{R}^2$ , which contains the desired imaging plane.

$$I \xrightarrow{D} T \xrightarrow{D'} \mathbb{R}^2 \quad (12)$$

Our goal is to obtain  $D'$ ; once we have done that we can assign the pixels of  $T$  to their true positions, and then assign the pixels of any aligned image  $I$  to their true positions by composing the two mappings. Whereas before we considered displacements and scan patterns as functions  $\mathbb{R}^1 \rightarrow \mathbb{R}^2$ , here we consider them as a locally smooth changes in coordinates  $\mathbb{R}^2 \rightarrow \mathbb{R}^2$ , even though they may not be globally injective and contain discontinuities at the beginning and end of each scan line. To obtain these  $\mathbb{R}^2 \rightarrow \mathbb{R}^2$  mappings, the mappings corresponding to individual line scans were interpolated bilinearly across groups of 4 pixels, so that  $D$  is locally bilinear. To explicitly state  $D$  for a given point  $(a, b)$  in  $I$ , we first find the times  $t_1, t_2, t_3, t_4$  such that by Eqs. (1) and (2) we have:

$$\begin{aligned} x(t_1) &= x(t_3) = [a], x(t_2) = x(t_4) = [a] + 1, y(t_1) = y(t_2) = [b], y(t_3) \\ &= y(t_4) = [b] + 1 \end{aligned} \quad (13)$$

We then define:

$$\begin{aligned} D_x(a, b) &= (1 - \{a\})(1 - \{b\})D_x(t_1) + \{a\}(1 - \{b\})D_x(t_2) \\ &\quad + (1 - \{a\})\{b\}D_x(t_3) + \{a\}\{b\}D_x(t_4) \\ D_y(a, b) &= (1 - \{a\})(1 - \{b\})D_y(t_1) + \{a\}(1 - \{b\})D_y(t_2) \\ &\quad + (1 - \{a\})\{b\}D_y(t_3) + \{a\}\{b\}D_y(t_4) \end{aligned} \quad (14)$$

Recall that  $[\dots]$  and  $\{\dots\}$  indicate integer (rounded down) and fractional parts of a number.

To determine the unknown displaced coordinates  $D'(T)$  for pixels of the template frame  $T$  in physical reality  $\mathbb{R}^2$ , we will use the image frames  $I$  aligned to the template through  $D$ . We can restate the given assumption (see Section 3) by saying that the average velocity of the excitation focus relative to the brain will be the same as in a displacement-free scan in the  $x$  direction, and 0 in the  $y$ :

$$\left\langle \left\langle \frac{d}{dt}(\text{focus position}) \right\rangle \right\rangle = \begin{bmatrix} w \cdot h/\tau \\ 0 \end{bmatrix} \quad (15)$$

where  $\langle \dots \rangle$  denotes a mean over all frames  $I$  aligned to  $T$  (including  $T$  itself). Note that both sides of Eq. (15) are velocities of the focus in physical reality  $\mathbb{R}^2$ .

Since the true velocity of the focus in  $\mathbb{R}^2$  should be  $w \cdot h/\tau$  horizontally and 0 vertically, can we simply invert the average estimated displacement velocity for  $D$  at each point in  $T$  to get the displacement velocity for  $D'$ , and thereby construct the desired mapping  $D'$ ? Not quite, since the composition of  $D$  and  $D'$  turns out not to

be a simple addition of velocities. However, this naïve approach is basically the right way of thinking about the problem.

Fix a point  $q$  in the template  $T$ . For any image  $I$  aligned to  $T$ , the motion of the excitation focus through the image  $I$  at  $D^{-1}(q)$  is by the definition of  $I$  constant and horizontal (Fig. 1a, bottom left), with velocity  $w \cdot h / \tau$  in pixels of  $I$ /second. Projecting this motion through the two displacement mappings in Eq. (12) yields  $d/dt$  (focus position), so we have

$$\frac{d}{dt}(\text{focus position}) = \frac{d}{dt} \left( D' \left( D \left( t \cdot \begin{bmatrix} w \cdot h / \tau \\ 0 \end{bmatrix} \right) \right) \right) \quad (16)$$

Applying the chain rule yields

$$\frac{d}{dt}(\text{focus position}) = dD'|_q \cdot dD|_{D^{-1}(q)} \cdot \begin{bmatrix} w \cdot h / \tau \\ 0 \end{bmatrix} \quad (17)$$

where  $dD'$  and  $dD$  are  $2 \times 2$  matrices of partial derivatives for the respective coordinate changes. The matrices take the forms:

$$dD|_q = \begin{bmatrix} 1 + t_{\text{pixel}} \cdot v_x \cdot (\tau/h) \cdot v_x & t_{\text{pixel}} \cdot v_y \cdot (\tau/h) \cdot v_x \\ t_{\text{pixel}} \cdot v_x \cdot (\tau/h) \cdot v_y & 1 + t_{\text{pixel}} \cdot v_y \cdot (\tau/h) \cdot v_y \end{bmatrix}, dD'|_q = \begin{bmatrix} 1 + t_{\text{pixel}} \cdot v'_x \cdot (\tau/h) \cdot v'_x & t_{\text{pixel}} \cdot v'_y \cdot (\tau/h) \cdot v'_x \\ t_{\text{pixel}} \cdot v'_x \cdot (\tau/h) \cdot v'_y & 1 + t_{\text{pixel}} \cdot v'_y \cdot (\tau/h) \cdot v'_y \end{bmatrix} \quad (18)$$

where  $v$  and  $v'$  are displacement velocities of  $D'$  and  $D$  at  $q$  and  $D^{-1}(q)$ .  $v$  is precisely known from the displacement estimated in aligning  $I$  to  $T$ , and the assumption of piecewise linearity in (4).  $v'$  is unknown.

Substituting (18) into (17), taking the expectation over all frames aligned to  $T$ , applying (15) and dividing by  $w \cdot h / \tau$  we have

$$\begin{bmatrix} 1 \\ 0 \end{bmatrix} = \left( Id_2 + \begin{bmatrix} v'_x \\ v'_y \end{bmatrix} \begin{bmatrix} t_{\text{pixel}} & \tau/h \end{bmatrix} \right) \cdot \begin{bmatrix} 1 + t_{\text{pixel}} \cdot \langle\langle v_x \rangle\rangle \\ t_{\text{pixel}} \cdot \langle\langle v_y \rangle\rangle \end{bmatrix} \quad (19)$$

where  $Id_2$  is the identity matrix. Solving for vector  $(v'_x, v'_y)$  we have

$$\begin{bmatrix} v'_x \\ v'_y \end{bmatrix} = - \begin{bmatrix} \langle\langle v_x \rangle\rangle \\ \langle\langle v_y \rangle\rangle \end{bmatrix} \frac{1}{1 + t_{\text{pixel}} \cdot \langle\langle v_x \rangle\rangle + (\tau/h) \cdot \langle\langle v_y \rangle\rangle} \quad (20)$$

Thus we have solved for the velocity of the unknown displacement  $D'$  at  $q$  in terms of the average velocities of the known displacement  $D$  at the points  $D^{-1}(q)$ . To determine  $D^{-1}(q)$  for a given point  $q$  we first find the square of four neighboring pixels mapping bilinearly through  $D$  to a quadrilateral containing  $q$ , and then find the point within the square mapping to  $q$  by solving the quadratic equations that describe an inverted bilinear mapping. When multiple preimages of  $q$  exist in the procedure for displacement estimation without a displacement-free template, all pre-image points contribute to the averages  $\langle\langle v_x \rangle\rangle$ ,  $\langle\langle v_y \rangle\rangle$ .

Since  $q$  was arbitrary, apply (20) to each pixel of  $T$  to get displacement velocity in pixels or  $\mu\text{m/s}$  across the template, which can then be summed cumulatively to yield  $D'$ . Note the similarity of our solution (20) to the naïve approach of an additive inverse; the multiplicative scaling factor appears since the composition of  $D$  and  $D'$  is not a simple addition of velocities.

After computing  $D'$  and the compositions  $D' \circ D$  for each frame, we can calculate the estimated position of each pixel in each frame,

in  $\mathbb{R}^2$  coordinates (corresponding to pixels of a nondisplaced scan pattern) or in microns. One can then compute an displacement-free average image by interpolating each aligned frame bilinearly to sample it at pixel centers in the template, and use that average as a template for another round of alignment. For template-less alignment, we used three iterations of this align-average process.

Since after convergence some line scans of the aligned frames  $I$  may be completely outside the boundaries of the template frame  $T$ , we can use the frames with lines farthest outside of  $T$ 's boundaries as template frames and repeat the template-free alignment to yield another displacement-free average image. Displacement-free average images can be aligned to each other using full-frame translations, yielding a final displacement-free average image larger than any individual imaging frame.

## Appendix B. Supplementary data

Supplementary data associated with this article can be found, in the online version, at doi:10.1016/j.jneumeth.2008.08.020.

## References

- Baker S, Matthews I. Lucas–Kanade 20 years on: a unifying framework. *Int J Comput Vision* 2004;56:221–55.
- Broser PJ, Schulte R, Lang S, Roth A, Helmchen F, Waters J, Sakmann B, Wittum G. Nonlinear anisotropic diffusion filtering of three-dimensional image data from two-photon microscopy. *J Biomed Opt* 2004;9:1253–64.
- Denk W, Strickler JH, Webb WW. Two-photon laser scanning fluorescence microscopy. *Science* 1990;248:73–6.
- Dombeck DA, Khabbaz AN, Collman F, Adelman TL, Tank DW. Imaging large-scale neural activity with cellular resolution in awake. *Mobile Mice Neuron* 2007;56:43–57.
- Feierabend M, Rückel M, Denk W. Coherence-gated wave-front sensing in strongly scattering samples. *Opt Lett* 2004;29:2255–7.
- Freund I, Deutsch M. Second-harmonic microscopy of biological tissue. *Opt Lett* 1986;11:94.
- Gradinaru V, Thompson KR, Zhang F, Mogri M, Kay K, Schneider MB, Deisseroth K. Targeting and readout strategies for fast optical neural control in vitro and in vivo. *J Neurosci* 2007;27:14231–8.
- Greenberg DS, Houweling AR, Kerr JN. Population imaging of ongoing neuronal activity in visual cortex awake rats. *Nature Neurosci* 2008;11:749–51.
- Hell S, Stelzer EHK. Properties of a 4Pi confocal fluorescence microscope. *J Opt Soc Am A* 1992;9:2159.
- Helmchen F, Fee MS, Tank DW, Denk W. A miniature head-mounted two-photon microscope. high-resolution brain imaging in freely moving animals. *Neuron* 2001;31:903–12.
- Kerr JN, de Kock CP, Greenberg DS, Bruno RM, Sakmann B, Helmchen F. Spatial organization of neuronal population responses in layer 2/3 of rat barrel cortex. *J Neurosci* 2007;27:13316–28.
- Kerr JN, Denk W. Imaging in vivo: watching the brain in action. *Nat Rev Neurosci* 2008;9:195–205.
- Kerr JN, Greenberg D, Helmchen F. Imaging input and output of neocortical networks in vivo. *Proc Natl Acad Sci USA* 2005;102:14063–8.
- Lucas B, Kanade T. An iterative image registration technique with an application to stereo vision. In: *Proceedings of the 7th international joint conference on artificial intelligence*; 1981. p. 674–9.
- Minsky M. Microscopy apparatus, US Patent 3,013,467; 1961.
- Sato TR, Gray NW, Mainen ZF, Svoboda K. The functional microarchitecture of the mouse barrel cortex. *PLoS Biol* 2007;5:e189.
- Sawinski J, Denk W. Miniature random-access fiber scanner for in vivo multiphoton imaging. *J Appl Phys* 2007;102:034701.
- Stosiek C, Garaschuk O, Holthoff K, Konnerth A. In vivo two-photon calcium imaging of neuronal networks. *Proc Natl Acad Sci USA* 2003;100:7319–24.